THE ARCHIVE OF MECHANICAL ENGINEERING

Vol. LI 2004 Number 3

Key words: *fracture mechanics, experimental methods, holographic interferometry, RCF, numerical calculations*

PAWEŁ PYRZANOWSKI[*)]

INFLUENCE OF A SUBSURFACE FATIGUE CRACK ON STRESS DISTRIBUTION DUE TO ROLLING CONTACT: EXPERIMENTAL VERIFICATION OF NUMERICAL RESULTS

The paper presents the results of experimental investigations into variations of the stress tensor components due to both the interaction between subsurface fatigue crack faces and rolling contact. The load assumed represents real interaction between the railway wheel and rail. The Grating Holographic Interferometry (GHI) method was employed. The results obtained were compared with those resulting from numerical simulations performed using FEM. The results reveal a strong influence exerted by shape, crack thickness distribution and roughness of the crack faces, respectively, on the distribution of displacement and stress tensor component fields. A new concept consisting in application of the effective crack thickness was proposed. The best agreement between experimental and numerical results was achieved in the case when the real crack shape, effective crack thickness and the friction coefficient of 0.3 were assumed.

1. Introduction

The paper is devoted to the problem of fatigue crack propagation in rail heads. This type of cracks is often called the RCF (Rail Contact Fatigue) one. The present work deals with the cracks called "squat", that appeared in rails in Poland as well as all over the world at the end of the twentieth century. Cracks of this type appeared in tracks in which about ten years earlier the rails made of steel of improved strength properties (resistant to abrasive wear) had been used.

[*)] *Institute of Aeronautics and Applied Mechanics, Warsaw University of Technology, Nowowiejska 24, 00-665 Warsaw, Poland; E-mail: pyrzan@meil.pw.edu.pl*

Fig. 1. shows a typical large-size singular crack, initiated on the rolling strip. In Fig. 1b, the crack boundaries, obtained by means of ultrasonic detection are introduced into the image of rail head with a crack. The length of this crack on the raceway is about 70 mm.

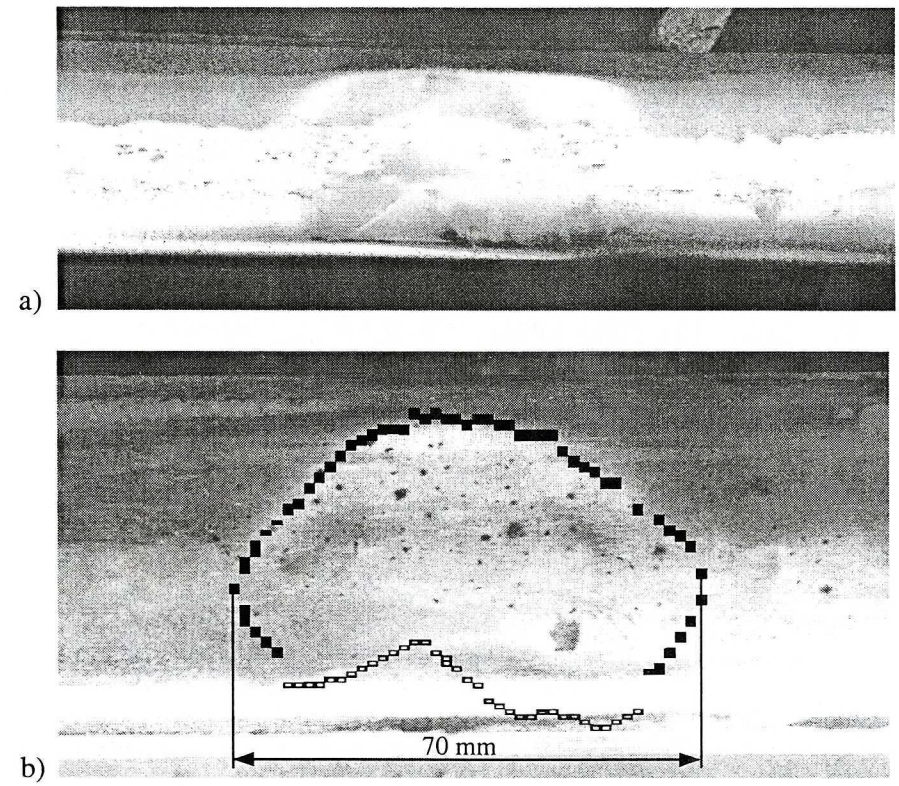

Fig. 1. Typical forms of a large size singular crack: a) top view; b) top view with the crack boundaries

Propagation of a crack of the "squat" type has been modelled in many works, e.g. [2], [3], [5], [7], [11], however, some problems still need attention and detailed explanation. In each hitherto existing model (two- or three-dimensional), real geometry of the wheel was assumed, in 3D models also geometry of the rail, the crack model however was oversimplified. Usually, the crack model had a form of line (2D models) or a semi-elliptical part of a plane (3D models). The thickness of the crack i.e. the distance between upper and lower faces was reduced to zero, and there was no friction between crack faces, or the friction coefficient was constant. In some papers however, for instance [1], the interaction between the crack faces happened to be very important and should be studied intensively. Since 3D models are very complicated, majority of the simulations in which the crack face interaction

was considered were performed using 2D models [12], [13], [14]. In these models, however, parameters of interaction between the crack faces were also assumed.

Reliable results of numerical simulations can be obtained only in the case when the values of interaction parameters between the crack faces result from experiments.

In the present study, the interaction between the faces of a subsurface fatigue crack developed in a railhead made of 900A steel has been measured using the Grating Holographic Interferometry (GHI) technique. A special experimental stand designed has allowed for application and a stepwise movement of constant rolling normal loads as well as for a full-field recording of the relative displacement vector components at two successive positions of the contact load. From the recorded interferometric fringe patterns, 2D maps of the displacement vector components were computed and the maps of the stress tensor components were determined. The study presented provides some extension of the experiments described in [8], [9], [17], [18], [19], [20], [24]. The objects of the study and experimental methods are the same as in [8], [19], [20], the paper, however, focuses on the maps of stress tensor components. The results obtained are compared with several numerical results, in which different shapes of the crack, crack thicknesses and friction coefficients were assumed.

The Stress Intensity Factors and the parameters that are required in numerical models of the development process of a fatigue crack were calculated for the numerical model of the crack, for which the best agreement between experimental and numerical results was achieved.

2. Experimental investigations

The present experimental investigations were performed under conditions representing the real load acting upon a rail.

2.1. Specimen

The examined object was a subsurface crack detected by an ultrasound thickness gauge in the real rail road after 12 years of exploitation. A special specimen was cut off from the rail head of UIC60 rail, made of 900A steel, the chemical constitution of which is given in Table 1. The specimen had a form of a plate (160 mm in length, 60 mm in height and 6 mm in thickness) cut off exactly below the wheel rolling trace. Fig. 2 presents the area from which the specimen was taken away and a specimen side view.

Table 1.

Chemical constitution of the 900A steel

element	C	Mn	Si	P	S	Al
mass fraction %	0.7÷0.76	1.0÷1.25	0.2÷0.4	<0.03	<0.025	<0.004

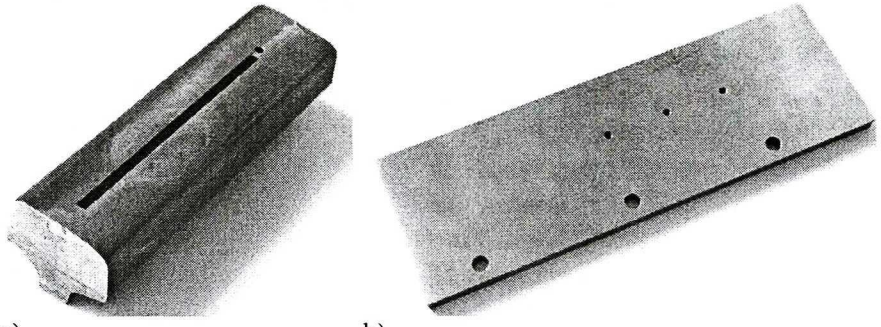

a) b)

Fig. 2. Specimen: a) the part of rail from which the specimen was cut off; b) side view of the specimen

The crack in the specimen had 70 mm in length, and was almost perpendicular to the specimen surface, being more or less parallel to the surface at a depth of 5.53÷6.97 mm. In the analysed area (25 mm of the crack from $x = -25$ to $x = 0$ at the right crack tip), its depth was 5.53÷6.17 mm. The crack shape and the analysed part of the crack are shown in Fig. 3.

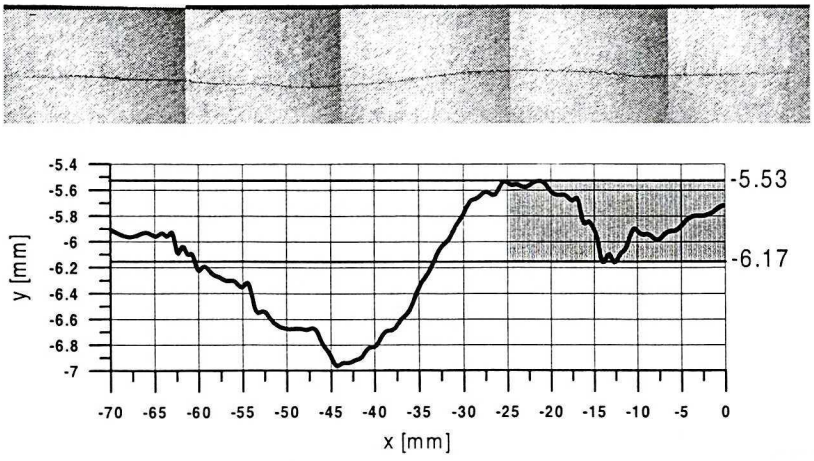

Fig. 3. Real shape of the specimen: a) photograph b) diagram of the crack depth

2.2. Experimental stand, load

Special experimental set-up was constructed to simulate real load of the rail. This set-up is shown in Fig. 4. The specimen was mounted to the clamping grips of the experimental stand. The whole support

allows the sample to move in the tangential direction when driven by the actuator. The circular cylinder rolls over samples upper surface. The segment of circular cylinder has a radius of 450 mm (as for the wheel system of modern railways standards) and allows loading the upper surface of the sample with a normal force. The magnitude of the load was controlled by a loading cell.

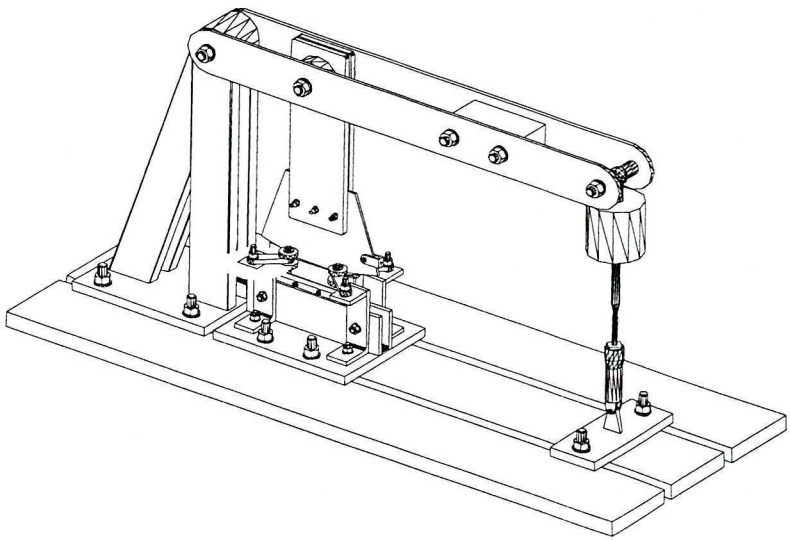

Fig. 4. Experimental stand

The specimen was subject to a loading procedure consisting of 14 steps. In the first 4 steps, only the normal load was applied at a distance of 31 mm to the left from the right crack tip (the analysed one). The maximum load was 8000 N and generated the maximum Hertz pressure of 330 MPa. Then, in the next 10 steps, the constant normal load was rolling along a distance of 30 mm. Fig. 5 shows the loading scheme. The results obtained at steps 1, 8 and 14, marked in the figure, will be discussed in detail in the next sections.

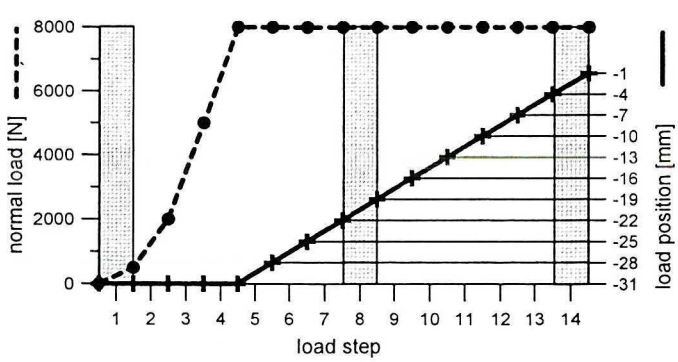

Fig. 5. Loading scheme

2.3. Experimental method

For 2D maps of the in-plane displacement vector components to be determined, a full-field optical method should be employed. In this case, the Grating Holographic Interferometry (GHI) method was used, since it allows small displacements (not exceeding the value of about 20 (m in one load step) being measured to be distinguished from the large-scale ones of the whole specimen (about 3 mm). The method is presented in detail in [23], [25].

In this method, a cross-line grating should be employed. Using a grating of a spatial frequency of 1200 lines/mm allows one to attain accuracy between 0.2 and 0.5 μm. The approach taken allows for recording and reconstruction, with the opposed beam arrangement, of a double-exposed image hologram. From the image, four independent fringe patterns are extracted at multiple off-axis angles, enabling one to compute the displacements. Fig. 6 presents four sample interferograms obtained at loading step 8.

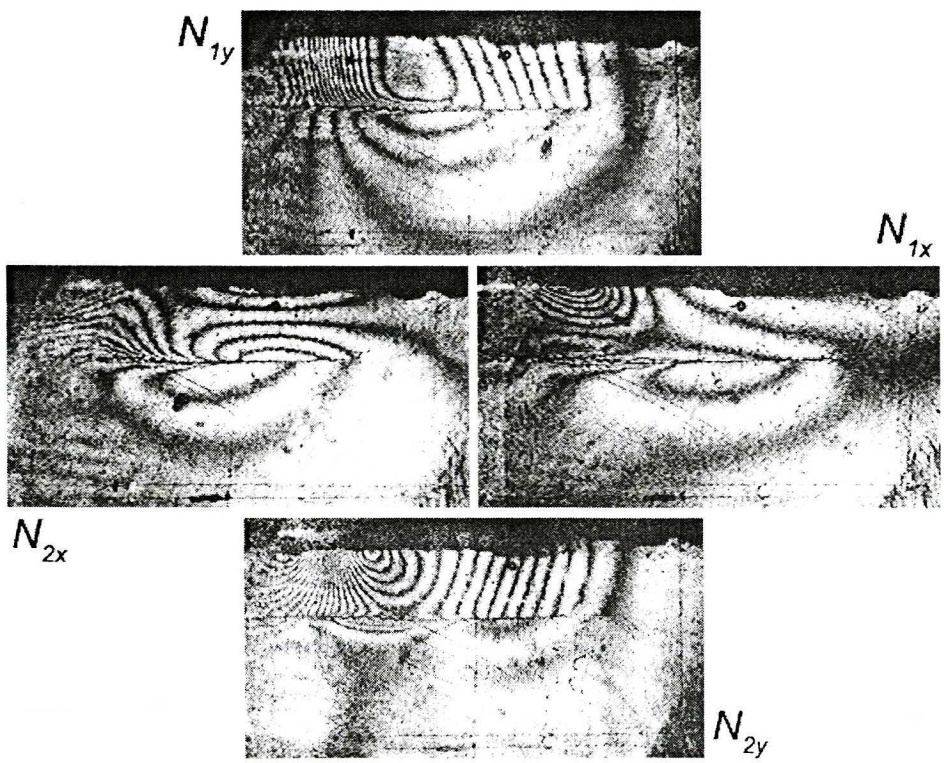

Fig. 6. Sample interferograms

2.4. Experimental Results

First, the maps of in-plane displacement vector components at all 14 steps were computed. Fig. 7 and 8 shows these components u (Fig. 7) and v (Fig. 8) at 1, 8 and 14 steps, respectively. The upper limit of the analysed area was located 0.5 mm below the specimen upper surface due to the grating boundaries. The results obtained at the points situated between $y = -5.5$ and $y = -6.25$ mm are not applicable, due to the real crack shape (F ig. 3), for which the results could be calculated only in the presented rectangular area. nThe line put into the above zone represents the real crack shape.

The displacement vector components shown in Fig. 7 and 8 were calculated using a grid with a space 0.25 mm × 0.25 mm. Then, the strain vector components were calculated assuming a base of 0.5 mm and a plane stress state; the stress vector components were calculated in the same way. Due to the features of the method applied, the area of analysis should be reduced by 0.25 mm from all sides.

The results obtained at 1, 8 and 14 steps are shown in Fig. 9, 10, 11, respectively.

The stresses measured at step 1 and shown in Fig. 9 are very small. In this case, only the normal load was increased from 0 to 500 N, and the centre of load was located at the point $x = -31$mm (6 mm left of the area of analysis left side). Therefore, the stress magnitudes reveal mainly the calculation errors, not greater then 20 MPa.

A very interesting case is shown in Fig. 10. The load was rolling from $x = -22$ to $x = -19$ mm. For $x \approx -16.5$ mm there occurs a very high concentration of stresses, clearly visible for the stress σ_{yy}. This concentration point appears on both crack surfaces: the upper and lower ones, which proves that it is not an arately. The stress variations during the rolling process become greater at the crack surface reaching the magnitude $\sigma_{yy} \approx -450$ MPa, while the magnitude computed in the case without a crack should be about $\sigma_{yy} \approx -80$ MPa (see Fig. 13 in the next section). The point $x = -16.5$ mm corresponds to a relatively big change in the crack depth (see Fig. 2). At the same point, also low concentration of the stress components σ_{xx} and σ_{xy} is visible. At the crack tip, stress changes are very small, therefore changes of the Stress Intensity Factors should also be small.

In the case shown in Fig. 11, the load was rolling from $x = -4$ to $x = -1$ mm. No stress concentration is visible at the point $x = -16.5$ mm since the crack at this position is opened and there is no interaction between the crack faces. The concentration, however, of σ_{yy} at the crack tip still exists, which proves that for this way of load location changes the SIF K_I values vary as well.

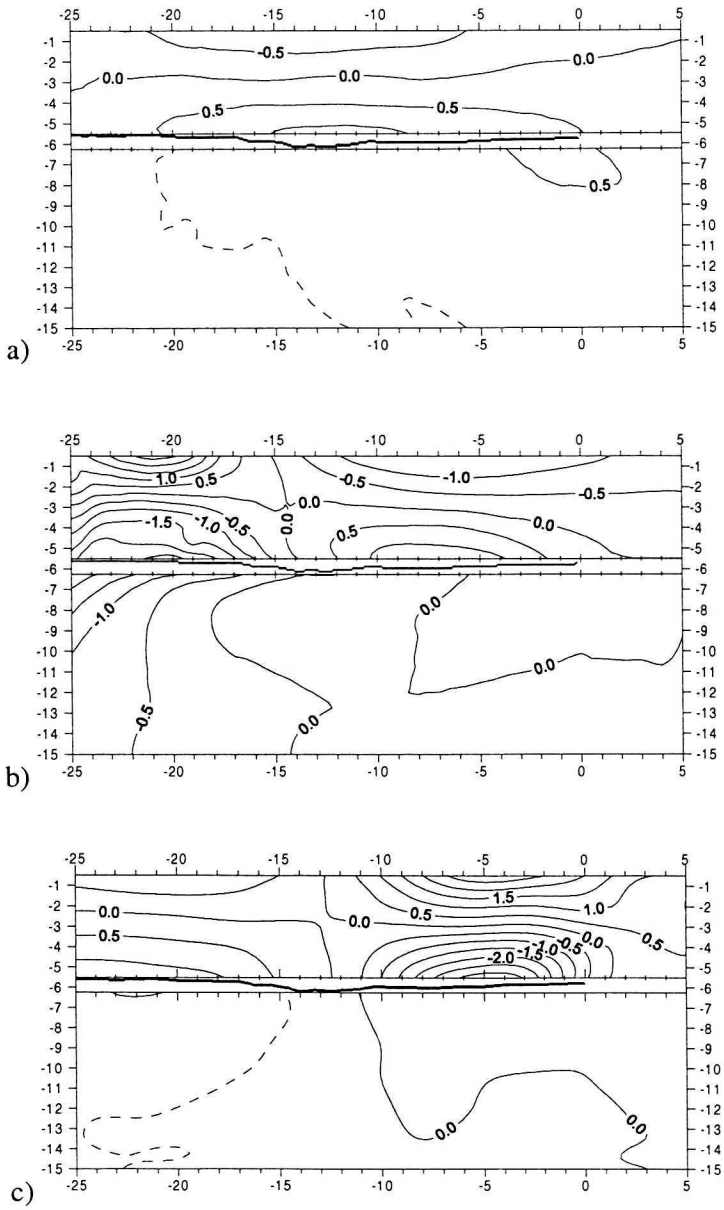

Fig. 7. Displacement vector components u [μm] at: a) 1; b) 8, and c) 14 steps, respectively, resulting from experiment

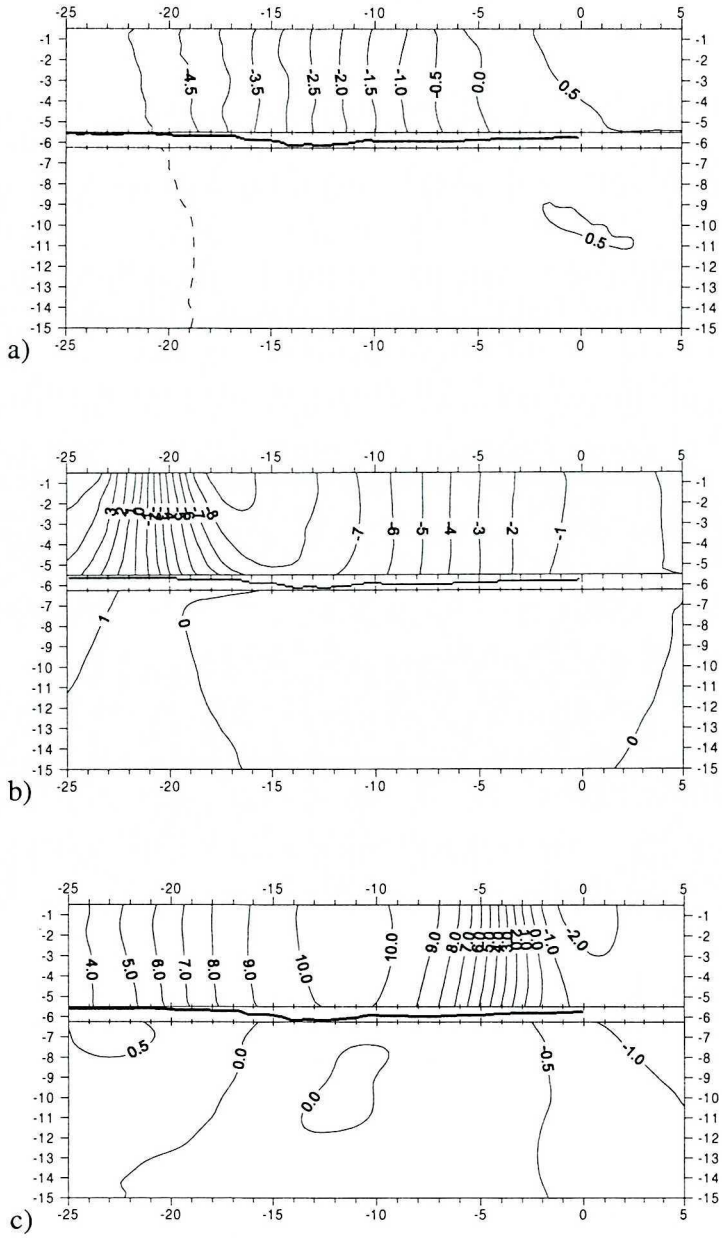

Fig. 8. Displacement vector components v [μm] at: a) 1; b) 8, and c) 14 steps, respectively, resulting from experiment

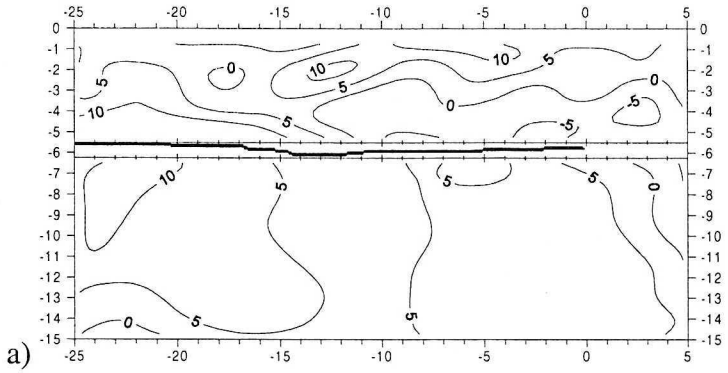

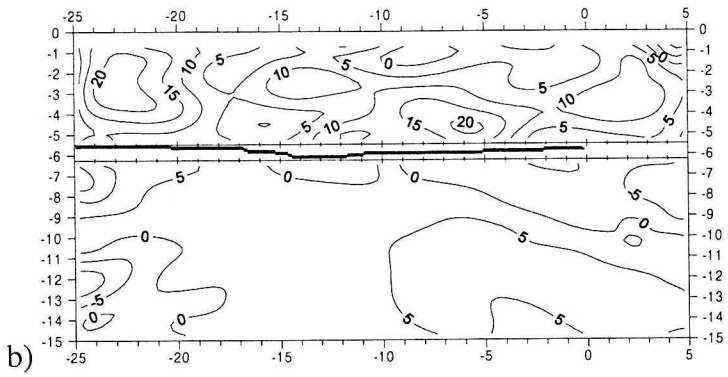

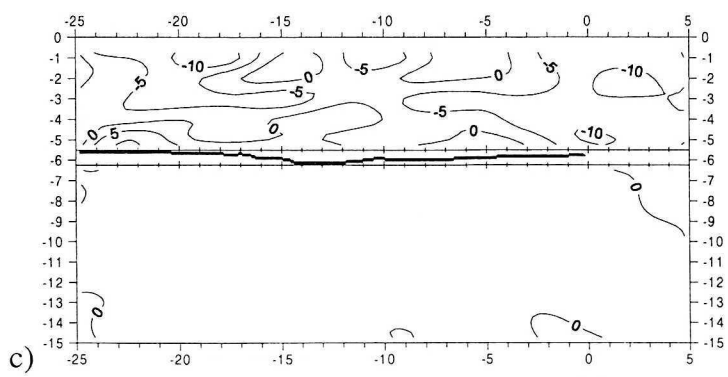

Fig. 9. Stress vector components [MPa] at step 1: a) σ_{xx}; b) σ_{yy}; c) σ_{xy}

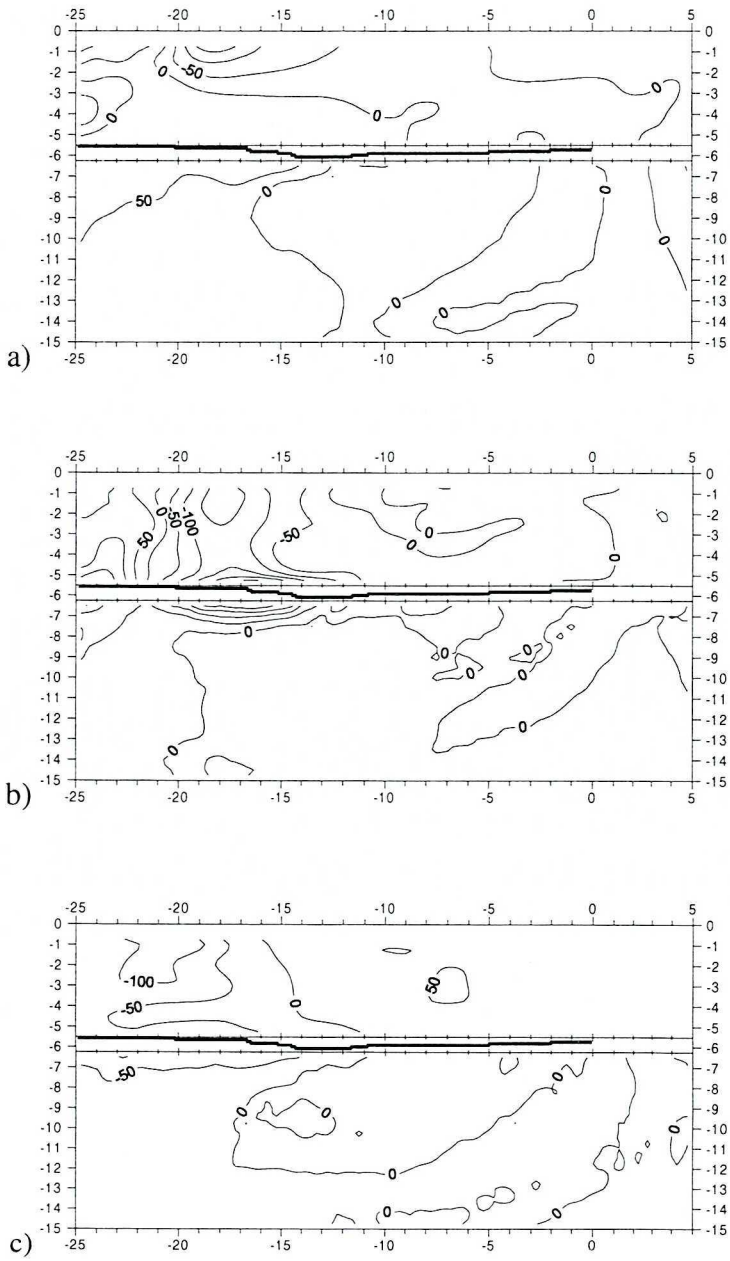

Fig. 10. Stress vector components [MPa] at step 8: a) σ_{xx}; b) σ_{yy}; c) σ_{xy}

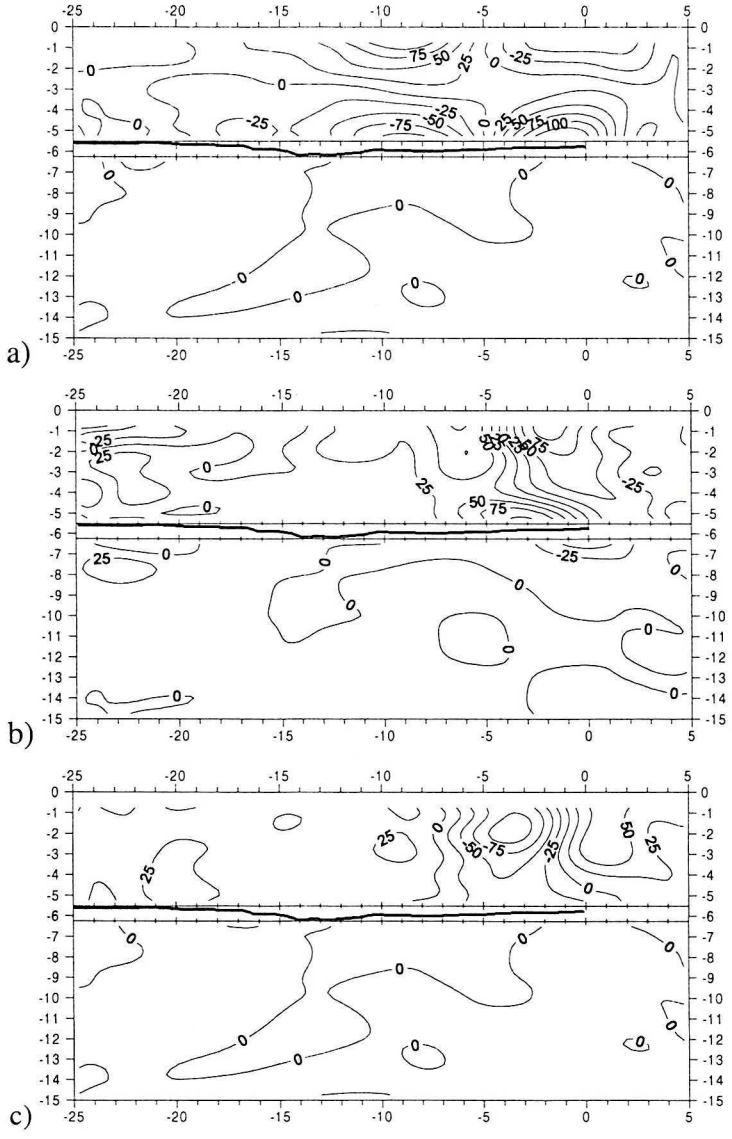

Fig. 11. Stress vector components [MPa] at step 14: a) σ_{xx}; b) σ_{yy}; c) σ_{xy}

3. Numerical investigations

Experimental investigations yielded very valuable results, on the other hand it was very difficult to perform the tests, especially in the cases of real 3D cracks. Numerical calculations can bring the results more easily, however, depend strongly on the modelling conditions assumed. In the case of

calculation of fracture parameters and crack face interactions, the parameters of crack face surfaces: shape, friction, distribution of crack thickness and roughness of crack faces are very important. The results discussed in this paper were obtained for different shapes of crack, friction coefficients, and crack thicknesses. The crack face roughness was neglected.

Numerical calculations were made using the FEM codes for a 2D model. The ANSYS software version 6.1 was employed. The quadrilateral elements on the crack faces had the edge of about 0.2 mm in length. The radius of a special crack tip element was 0.05 mm. Fig. 12 shows FE mesh at the right side of the crack (Fig. 12a) and near the crack tip (Fig. 12b). The lower edge of the specimen was fixed ($u = v = 0$). The normal (vertical) load force and the displacement of the rolling cylinder was applied to the axle of the cylinder.

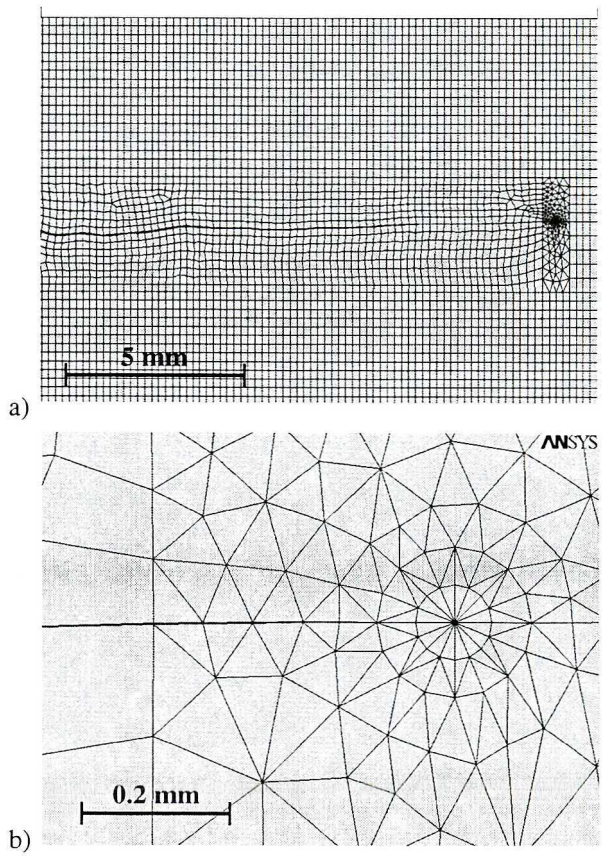

Fig. 12. Finite element mesh: a) at the right side of the crack; b) near the crack tip

The computations were done also in the case with no crack in the rail. The resulting maps of stresses are shown in Fig. 13, and the results could be

compared with those obtained in the cases with the crack (shown in Figs. 19 and 20). The differences between results from Fig. 13, 19 and 20 illustrate the influence of the crack on the distribution of stresses.

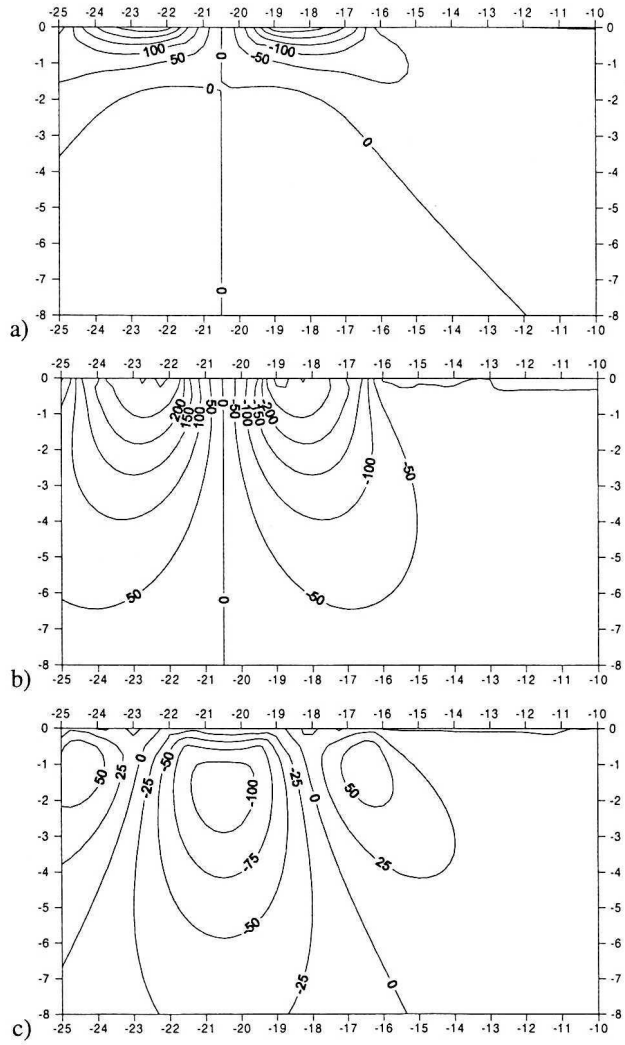

Fig. 13. Numerically obtained values of the stress vector components [MPa] obtained in the case with no crack at step 8: a) σ_{xx}; b) σ_{yy}; c) σ_{xy}

3.1. Crack face interaction cases assumed

Since the experiment aimed mainly at verification of numerical investigation results, the calculations had to be done in different cases, depending on the conditions under which the tests were performed. The following cases were calculated:

1. Constant-depth crack (5.7 mm), no crack thickness, no friction;
2. Constant-depth crack (5.7 mm), no crack thickness, the friction coefficient of 0.3;
3. Constant-depth crack (5.7 mm), a sinusoidal course of the crack thickness, no friction;
4. Constant-depth crack(5.7 mm), a sinusoidal course of the crack thickness, the friction coefficient of 0.3;
5. Crack of the real depth (measured), no crack thickness, the friction coefficient of 0.3;
6. Crack of the real depth (measured), a sinusoidal course of the crack thickness, no friction;
7. Crack of the real depth (measured), a sinusoidal course of the crack thickness, the friction coefficient of 0.3;
8. Crack of the real depth (measured), the effective crack thickness, no friction;
9. Crack of the real depth (measured), the effective crack thickness, the friction coefficient of 0.3.

Cases 1 and 2 are typical and therefore are most common in the computations performed till now. The friction coefficient value of 0.3 was assumed from experiment described in [17], where also a nonzero crack thickness was observed. A simple assumption of the thickness sinusoidal distribution seems to be reasonable, since it increases in a linear way assuming the value of 0 at the crack tips ($x = 0$ and $x = -70$ mm) and the value of 1 μm at the points $x = -0.2$ mm and $x = -69.8$ mm, respectively. Then, from $x = -0.2$ mm to $x = -69.8$ mm the thickness grows following a sinusoid with the maximum of 50 μm at $x = -35$ mm. The term "real (measured)" depth used in the description of computation cases means the real crack profile being measured (see Fig. 3). Since the results obtained in cases 1÷7 were not in a satisfactory agreement with the experimental results, it was necessary to find a better distribution of the crack thickness. The idea of effective crack thickness has been put forward.

3.2. Effective crack thickness

Numerical calculations show that the results obtained depend strongly on the assumed crack thickness. Since a numerical model assumed should correspond to the reality, the crack thickness should be measured. Usually it is not possible, since it is a destructive test, and reliable results are very difficult to arrive at. In view of the above, it is not necessary to have the whole crack thickness distribution, knowing of thickness values at the required points seems to be enough. To this end, the crack faces opening/closing for each loading step were taken

from experiment. Crack opening/closing is the difference between displacement vector y in the upper and lower crack face. The effective crack thickness was then calculated as the maximum crack faces closing for each load position. Of course, the value of the crack thickness is positive, while crack opening/closing is negative (because the crack is closed under the load). The concept is illustrated in Fig. 14. The effective crack thickness could depends on loading conditions and should be calculated separately in each case of loading.

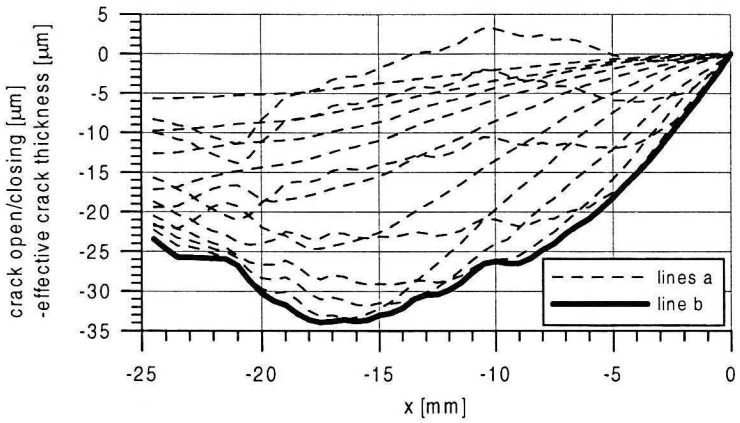

Fig. 14. Calculation of the effective crack thickness:
lines a – crack opening/closing at steps 1÷14
line b – effective crack thickness

The effective crack thickness could be calculated only for the area under consideration (in this case for $x >= -25$ mm). For the remaining part of the crack ($x < -25$ mm), the crack thickness was assumed in the way shown in Fig. 15.

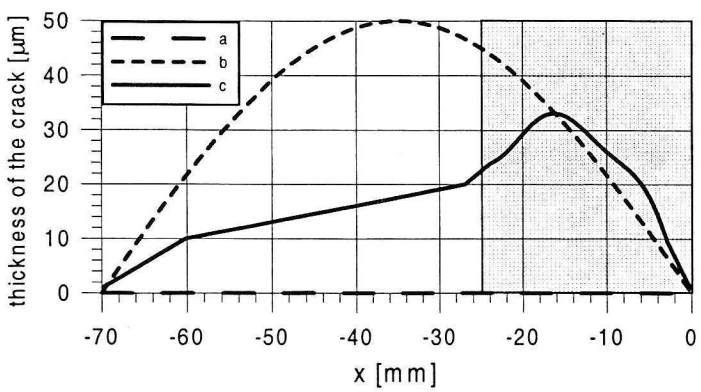

Fig. 15. Thickness of the crack analyzed in the numerical investigations
a) without thickness; b) sinusoidal thickness; c) effective thickness

3.3. Numerical results

The values of Stress Intensity Factors (SIFs) resulting from calculations are of crucial importance in numerical investigations into the crack development. Since the initial crack thickness was greater then zero in the calculations presented in section 3.1, the SIF K_I value was nearly equal to zero. Therefore, the most important factor consists in the value of SIF K_{II}.

Fig. 16 shows the distribution of Stress Intensity Factor K_{II} as a function of the load position that result from numerical calculations. The diagram presents only three most interesting results obtained in cases 1, 8 and 9 described in section 3.1. Case 1 is the most common in investigations of a linear crack with no thickness and no friction between its faces. Although there is no friction, the amplitude of the SIF K_{II} is very small due to the zero thickness assumed. The maximal value of amplitude of K_{II} was obtained in case 8, when the crack had the real shape, and effective thickness and no friction were assumed. This amplitude was about 80% higher then in case 1. Case 9 was calculated under the same conditions as case 8, except the friction coefficient, which was equal to 0.3.

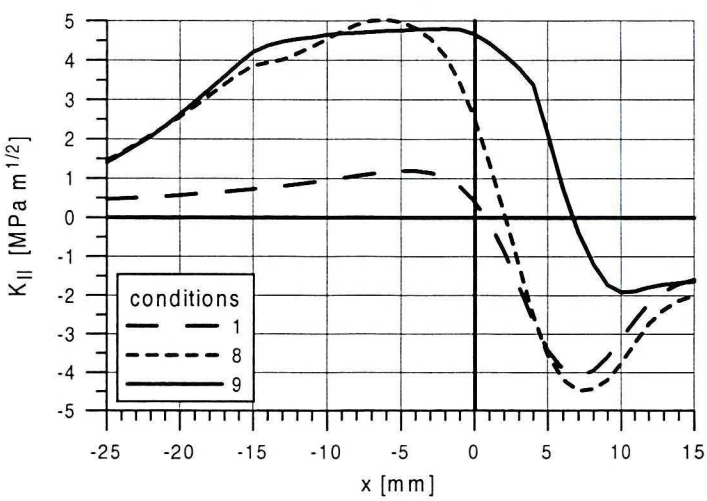

Fig. 16. Sample distributions of the Stress Intensity Factor K_{II} under different crack conditions

The values of Stress Intensity Factors are very useful in calculation of the crack growth rate. For the steel used for rails in Great Britain, of the properties similar to those of 900A, for a multi-mode crack growth the following model was proposed [4]:

$$\frac{da}{dN} = 0.000614 \cdot \left(\Delta K_{eq}^{3.21} - 4^{3.21}\right) \quad \frac{\text{nm}}{\text{cycle}} \tag{1}$$

$$\Delta K_{eq}^{2} = \Delta K_{I}^{2} + \left[\frac{614}{507} \cdot \Delta K_{II}^{3.21}\right]^{\frac{2}{3.74}} \quad \text{MPa}\sqrt{\text{m}} \tag{2}$$

The above equations were employed in calculations, the results of which are presented in Table 2, in terms of the minimal and maximal values of K_{II}, their amplitudes ΔK_{II} and crack growth rate for every 9 cases which were analysed. Cases 1, 8 and 9 are marked with boldface numbers.

Table 2.

Results of numerical calculations

crack conditions	**1**	2	3	4	5	6	7	**8**	**9**
K_{IImin} [MPa]	−4.09	−2.70	−3.07	−1.49	−2.75	−4.84	−2.45	−4.48	−1.92
K_{IImax} [MPa]	1.19	2.60	2.97	3.47	2.44	4.37	4.63	5.03	4.80
ΔK_{II} [MPa]	**5.28**	5.30	6.04	4.96	5.19	9.21	7.08	**9.51**	**6.72**
da/dN [m^{-12}/cycle]	**18.3**	19.05	0.1	7.1	15.0	275.7	106.5	**306.0**	**85.2**

The 80 per-cent-difference in amplitudes of K_{II} obtained in cases 1 and 8 resulted in much higher change in the crack growth rate. The growth rate obtained in case 8 was about 17 times higher than that in case 1.

Since the obtained crack growth rates differ so greatly, only one of them, the most acceptable one, should be chosen basing on the experimental results. At each loading step, the numerical results should be compared with the experimental ones, especially at steps 5÷14, when the load is rolling over the specimen upper surface. The best result can be obtained from comparison between 2D maps of the displacements u and v and, of course, microslips and crack opening/closing. For the sake of clarity and simplicity, only the results obtained in case 9 are presented, since in that case the smallest difference between the experimental and numerical results emerges. Fig. 17 presents 2D maps of the displacements u and v, which can be compared with the diagrams presented in Fig. 7b and 8b. Fig. 18 shows the microslips and crack opening/closing resulting from experiment and numerical simulation, respectively, for the start and the end of loading step 8.

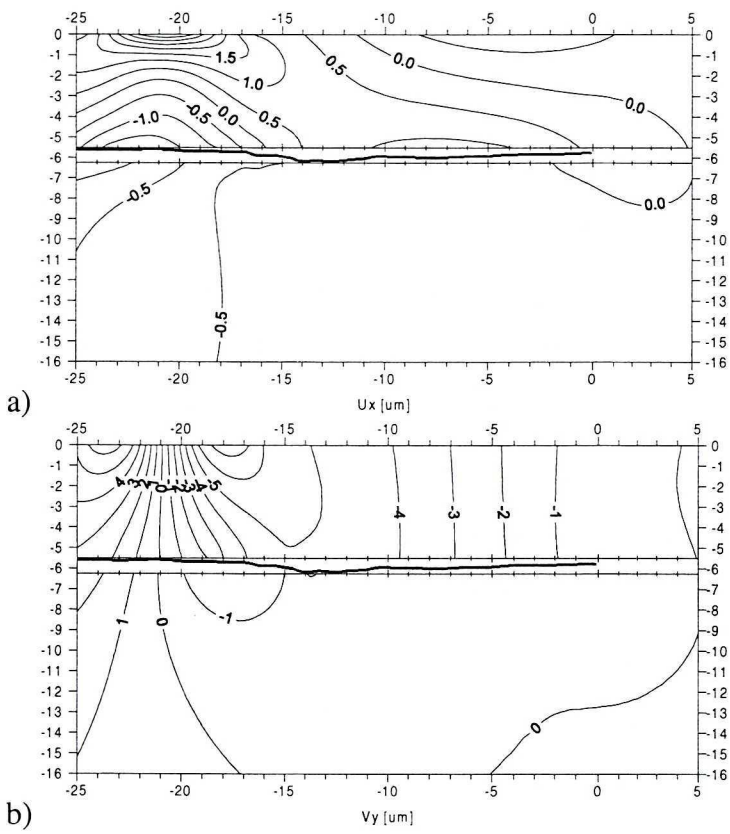

Fig. 17. Numerically obtained values of the displacements in the 9 case of the crack conditions a) u [μm] component b) v [μm] component

The experimental and numerical results are similar, but not the same. It is possible that a better agreement can be attained when the crack face roughness is taken into account. A significant influence of this factor was indicated by other authors (e.g. [6], [10], [20], [21]), and primary tests have already yielded promising results. These will be presented in the following papers. In the mentioned tests, the parameters of crack face roughness given in [15], [16] were applied. The second source of difference between the experimental and numerical results could be an inaccurate image of the real geometry in FE model. Real specimen is three dimensional and the geometry of the crack in the front and in the back side of specimen is not the same (the crack is not exactly normal to the plane of specimen). Consequently also out-of-plane displacement vector components were observed in the experiment. Numerical investigations were done for 2D model which regards only in-plane displacements.

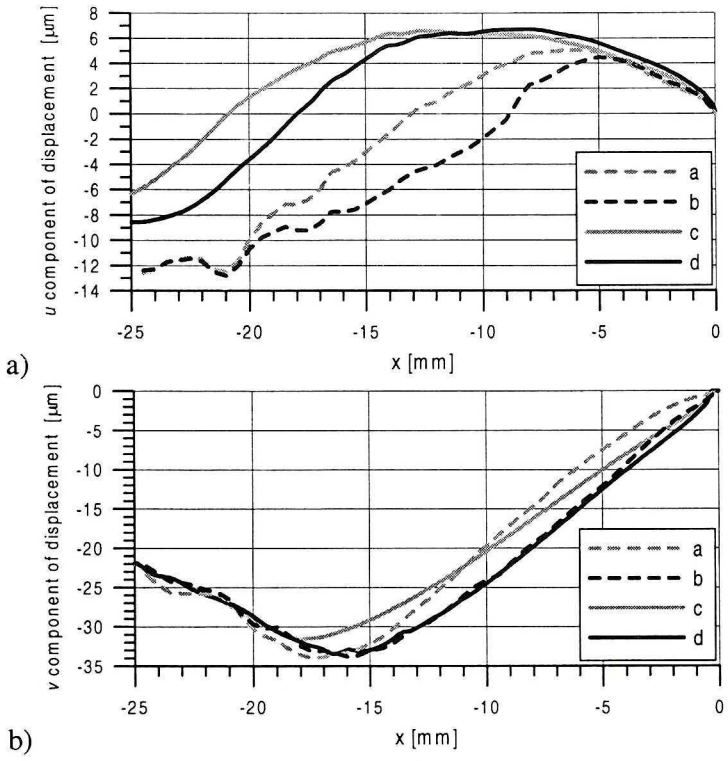

Fig. 18. Comparison between the courses of a) microslips b) crack opening/closing represented by:
line a – experimental results for the start of step 8;
line b – experimental results for the end of step 8;
line c – numerical results for the start of step 8;
line d – numerical results for the end of step 8

Fig. 19 and Fig. 20 present the stress tensor components for the start (Fig. 19) and the end (Fig. 20) of loading step 8 resulting from numerical simulations. Although there is no roughness of the crack faces introduced, the application of effective crack thickness results in a small concentration of stresses between $x = -22$ mm and $x = -16$ mm, similar (but smaller) to that obtained from experiment. Considerable influence of roughness (not regarded in numerical model) can be the reason of differences between experimental and numerical results.

Comparison of stresses for the numerically obtained results without crack (Fig. 13) and with crack (Fig. 19 and 20) shows very high influence of the crack. It is caused by discontinuity of the material in the crack. It causes crack opening or closing, microslips of crack faces and consequently discontinuity of stresses' transfer.

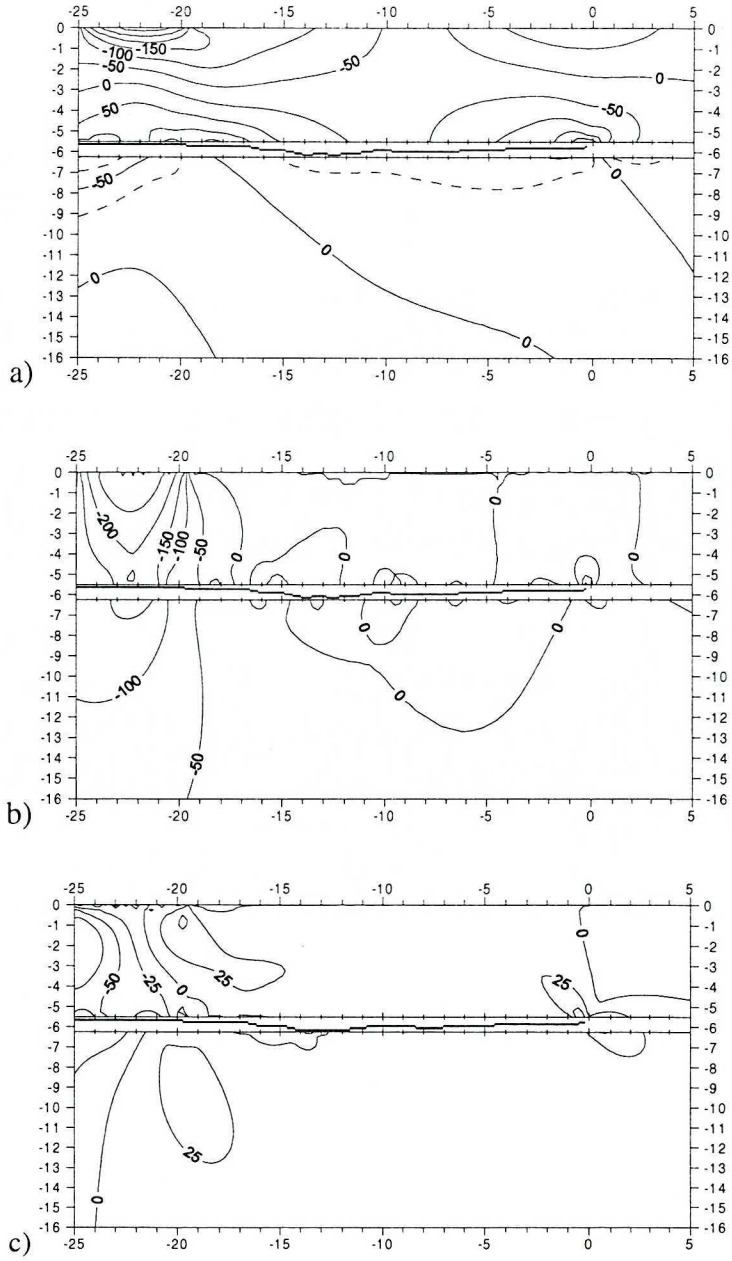

Fig. 19. Stress vector components [MPa] for the start of step 8 resulting from numerical simulation: a) σ_{xx}; b) σ_{yy}; c) τ_{xy}

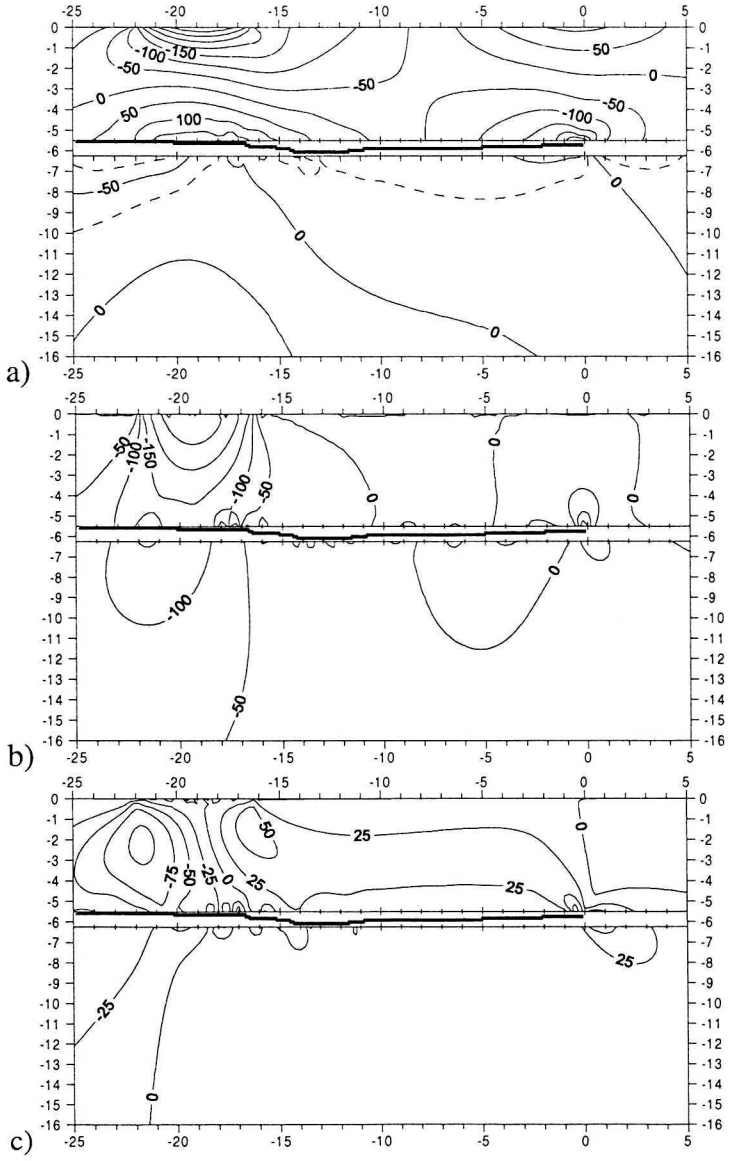

Fig. 20. Stress vector components [MPa] for the end of step 8 resulting from numerical simulation: a) σ_{xx}; b) σ_{yy}; c) τ_{xy}

4. Conclusions

The experimental and numerical investigations conducted allowed some interesting conclusions to be drawn:

1. The Grating Holografic Interferometry (GHI) approach employed yielded reliable measurement results of the displacement vector components u and

v in the crack vicinity, microslips and crack opening/closing. The accuracy from 0.2 to 0.5 μm was attained depending on the value of displacement. The full-field maps of displacements allow one to calculate the maps of stresses in the crack vicinity.

2. The constructed experimental stand allowed for observation of the process of load rolling allowing also for observation and measurement of the crack faces microslips and dilatation during this process.
3. Observation of the crack closing while rolling makes it possible to calculate the effective crack thickness, for which the best results of numerical calculations were obtained.
4. The results obtained prove a strong influence of the crack face roughness on the distribution of stress tensor components. The stresses observed on the crack faces can be much higher than the maximum Hertz pressure in the contact zone.

The work was done as a part of a grant No. 8 T07A 012 20 sponsored by the State Committee for Scientific Research.

Manuscript received by Editorial Board, December 25, 2004;
final version, July 23, 2004.

REFERENCES

[1] Bower A. F.: The influence of crack face friction and trapped fluid on surface initiated rolling contact fatigue cracks. ASME Journal of Tribology, 110, 1988, pp. 704÷711.

[2] Bogdański S., Olzak M., Stupnicki J.: Numerical stress analysis of rail contact fatigue cracks, Wear, 191, 1996, pp. 14÷24.

[3] Bogdański S., Olzak M., Stupnicki J.: Numerical Modelling of a 3D rail RCF "squat"-type crack under operating load, Fatigue & Fracture of Engineering Materials & Structures, 1998, pp. 923÷935.

[4] Bogdański S., Stupnicki J., Brown M. W., Cannon D. F.: A two dimensional Analysis of Mixed-Mode Rolling Contact Fatigue Crack Growth in Rails. Proc. Of 5th International Conference on Biaxial/Multiaxial Fatigue & Fracture, Cracow, Poland, 1997, pp. 189÷206.

[5] Duborg M. C., Kalker J. J.: Crack behaviour under rolling contact fatigue, Rail Quality and Maintenance for Modern Railway Operation, Kluver Academic Publisher, 1993.

[6] Gray G. T., Williams C. J., Thompson A. W.: Roughness Induced Crack Closure: An Explanation for Microstructurally Sensitive Fatigue Crack Growth. Metallurgical Transaction A, vol. 14A, 1983, pp. 421÷431.

[7] Kaneta M., Matsuda K., Murakami K., Nashikawa H.: A possible Mechanism for Rail Dark Spot Defects. Proc. of World Tribology Congress, London, September 1997.

[8] Morbarigazzi C., Stupnicki J.: Measurement of microslips of subsurface fatigue crack faces due to rolling loads. Proceedings of YSESM, Milano-Marittima, 2003, pp. 91÷92.

[9] Mruk I., Pyrzanowski P., Stupnicki J.: Study of fatigue crack faces interaction in the cases of pure shear and shear with compression. Proc. of 19th Symposium on Experimental Mechanics of Solids, Jachranka, 2000, pp. 398÷403, (*in polish*).

[10] Nong Chen: An Analytical Model Which Combines Roughness and Plasticity Induced Fatigue Crack Closure. Ph.D. Thesis, University of Ilinois at Urbana-Champaign, 1997.

[11] Olzak M., Stupnicki J., Wójcik R.: Numerical analysis of surface crack propagating in rail-wheel contact zone. In: Rail Quality and Maintenance for Modern Railway Operation, ed. J. J. Kalker, D. F. Cannon and D. Oringer, Kluwer Acad. Press, The Netherlands, 1992, pp. 385÷395.

[12] Olzak M., Stupnicki J.: Wpływ modelu oddziaływania brzegów szczeliny powierzchniowej na wartości i przebieg amplitudy współczynników intensywności naprężeń. Mat. XVII Symp. Zmęczenia Materiałów i Konstrukcji, Bydgoszcz Pieczyska, 1998, pp. 227÷232 (*in polish*).

[13] Olzak M., Stupnicki J.: The influence of crack faces interaction model on the results of numerical study of stress intensity factors for the surface breaking cracks in race way. International Conference Contact Mechanics 1999, Stuttgart 1999, pp. 109÷118.

[14] Olzak M., Stupnicki J.: Fluctuation of the Stress Intensity Factors under a load rolling over a race-way with crack. Part I: Crack with uneven faces, Part II: Crack with initial clearence and surface layers of changed mechanical properties. Proc. of VII Conference on Fracture Mechanics, Kielce-Cedzyna, 1999, pp. 109÷123 (*in polish*).

[15] Pyrzanowski P., Mruk I.: Structure of the face of the "squat"-type fatigue crack in the head of the rail (*in Polish*). Mechanika 68 (1999). Materiały VII Krajowej Konferencji Mechaniki Pękania Kielce-Cedzyna, 1999, pp. 77÷82 (*in polish*).

[16] Pyrzanowski P., Mruk I.: Investigation of "squat"-type of crack development in a heads of a rail. Proc. of 17th Danubia-Adria Symposium on Experimental Methods in Solid Mechanics, 2000, Prague, Czech Republic, pp. 281÷284.

[17] Pyrzanowski P., Stupnicki J.: Interaction between the faces of a "squat"-type fatigue crack determined by use of the grating holographic interferometry. Proceedings of 14th European Conference on Fracture, part III Kraków, 2001, pp. 713÷723.

[18] Pyrzanowski P., Stupnicki J.: Study of Interaction of Squat-type Crack Faces Using Grating Holographic Interferometry. Proceedings of 18th Danubia-Adria Symposium on Experimental Methods in Solid Mechanics, 2001, Steyr, Austria, pp. 17÷19.

[19] Pyrzanowski P., Stupnicki J.: Microslips of crack faces of a subsurface fatigue crack in a railway raceway under a rolling loady. Proceedings of 19th Danubia-Adria Symposium on Experimental Methods in Solid Mechanics, 2002, Polanica Zdroj, Poland, pp. 166÷167.

[20] Pyrzanowski P., Stupnicki J.: Interaction between the crack faces of subsurface fatigue cracks due to normal and tangential loads. Proceedings of 20th Danubia-Adria Symposium on Experimental Methods in Solid Mechanics, 2003, Györ, Hungary, pp. 190÷192.

[21] Ravichandran K. S.: Theoretical Model for Roughness Induced Crack Closure. International Journal of Fracture, vol. 44, 1990, pp. 97÷110.

[22] Surech S., Ritchie R. O.: A Geometrical Model for Fatigue Crack Closure Induced by Surface Roughness. Metallurgical Transaction A, vol. 13A, 1982, pp. 1627÷1631.

[23] Szpakowska M.: Determination of the Rigidity of a Layer Containing a Fatigue Crack Under Normal and Tangential Loads Acting Simultaneously. Ph.D. Thesis, Warsaw University of Technology, Warsaw, 2000 (*in polish*).

[24] Szpakowska M., Pyrzanowski P., Stupnicki J.: Interference of fracture surfaces observed by means of optical methods for the cracks subjected to shear and compression. Proc. of IUTAM Symposium Advanced Optical Methods and Application in Solid Mechanics, Poitiers, France 1998, Vol. 2, L. 37, pp. 1÷12.

[25] Tu M., Gielisse P. J., Xu W.: Grating Holographic Interferometry. Experimental Mechanics, 1997, 37 (2), pp. 188÷196.

Wpływ podpowierzchniowej szczeliny zmęczeniowej na rozkład naprężeń podczas przetaczania obciążenia – eksperymentalna weryfikacja wyników numerycznych

Streszczenie

W pracy przedstawiono eksperymentalnie otrzymane rozkłady zmian naprężeń będące wynikiem oddziaływania szczeliny podpowierzchniowej i obciążenia zewnętrznego – przetaczanego po powierzchni próbki. Sposób obciążenia odpowiadał rzeczywistemu obciążeniu szyny kolejowej przez koło. W eksperymencie użyto metody siatkowej interferometrii holograficznej. Uzyskane wyniki porównywane były z uzyskanymi w wyniku symulacji numerycznych przy różnych kształtach i grubościach szczeliny oraz współczynnikach tarcia pomiędzy brzegami szczeliny. Wykazano bardzo duży wpływ tych czynników na uzyskane wyniki. Najlepszą zgodność uzyskano dla obliczeń przy rzeczywistym – zmierzonym na modelu kształcie szczeliny, współczynniku tarcia 0.3, oraz efektywnej grubości szczeliny. W pracy zdefiniowano tę wielkość oraz zaproponowano sposób jej wyznaczania.